(When) Can Wave Heating Balance Optically Thin Radiative Losses in the Corona?

I. De Moortel[1,2] and T. A. Howson[1]
[1] School of Mathematics and Statistics, University of St Andrews, St Andrews, Fife, KY16 9SS, UK; ineke.demoortel@st-andrews.ac.uk
[2] Rosseland Centre for Solar Physics, University of Oslo, PO Box 1029 Blindern, NO-0315 Oslo, Norway

Abstract

Why the atmosphere of the Sun is orders of magnitudes hotter than its surface is a long standing question in solar physics. Over the years, many studies have looked at the potential role of magnetohydrodynamic (MHD) waves in sustaining these high temperatures. In this study, we use 3D MHD simulations to investigate (driven) transverse waves in a coronal loop. As the boundary-driven transverse waves propagate along the flux tube, the radial density profile leads to resonant absorption (or mode coupling) and phase mixing in the boundaries of the flux tube and the large velocity shears are subject to the Kelvin–Helmholtz instability (KHI). The combination of these effects leads to enhanced energy dissipation and wave heating. Considering both resonant and nonresonant boundary driving as well as different densities for the flux tube, we show that only wave heating associated with a resonant driver in a lower-density loop (with a loop core density $\sim 5 \times 10^{-13}$ kg m^{-3}) is able to balance radiative losses in the loop shell. Changing the model parameters to consider a denser loop or a driver with a nonresonant frequency, or both, leads to cooling of the coronal loop as the energy losses are greater than the energy injection and dissipation rates.

Unified Astronomy Thesaurus concepts: Solar coronal loops (1485); Solar coronal heating (1989); Solar coronal waves (1995)

1. Introduction

The solar corona is the hottest layer of the Sun's atmosphere and the physical processes that maintain the high temperatures are the subject of one of the great unsolved problems in astrophysics: the coronal heating problem. Since the discovery of the hot corona, almost a century ago, a wide variety of mechanisms have been proposed for driving the required energy release in the Sun's atmosphere (e.g., see reviews by Klimchuk 2006; Parnell & De Moortel 2012; Reale 2014; Klimchuk 2015; Viall et al. 2021). Generally, these are categorized into two broad groups; DC heating (e.g., reviewed by Wilmot-Smith 2015) and AC heating (e.g., reviewed by Arregui 2015; Van Doorsselaere et al. 2020). In either case, energy must be transferred to small length scales, where it can be dissipated (e.g., due to magnetic reconnection and/or ohmic/viscous heating). In this article, we focus on energy release associated with magnetohydrodynamic (MHD) waves in the solar corona (AC heating).

Contemporary, high resolution imaging telescopes have revealed an abundance of wave energy in a huge variety of structures throughout the Sun's atmosphere (e.g., Khan & Aurass 2002; De Pontieu et al. 2012; Kim et al. 2012; Duckenfield et al. 2019; Morton et al. 2021). This highlights the possibility that wave energy may be important for maintaining the temperature of the atmospheric plasma (see also De Moortel & Pascoe 2012; McIntosh & De Pontieu 2012; Pant et al. 2019). While the observed oscillations generally exist on large scales (they are more easily observed given resolution constraints), a variety of plasma processes are known to promote the transfer of wave energy to small scales where dissipative processes can become effective. These include resonant absorption (Ionson 1978; Davila 1987; Hollweg & Yang 1988;

Ruderman & Roberts 2002; Goossens et al. 2006), phase mixing (Grossmann & Tataronis 1973; Hasegawa & Chen 1974; Heyvaerts & Priest 1983) and the Kelvin–Helmholtz instability (KHI; e.g., Chandrasekhar 1961; Browning & Priest 1984; Terradas et al. 2008; Antolin et al. 2015).

These processes need not occur in isolation and can coexist to drive energy dissipation throughout coronal structures by transferring wave energy from bulk (large) scales to small scales. The general paradigm is as follows:

1. Transverse kink waves in dense coronal loops decay rapidly due to resonant absorption (e.g., see reviews by Nakariakov & Verwichte 2005; Goossens 2008; Ruderman & Erdélyi 2009). The existence of a resonance in the boundary of an oscillating flux tube transfers energy from the kink mode to localized azimuthal Alfvén waves.
2. These azimuthal oscillations in the flux tube boundary undergo phase mixing due to a transverse gradient in the local Alfvén speed/frequency.
3. In the case of standing waves, the velocity shear that forms across magnetic field lines can become unstable to the KHI (e.g., Browning & Priest 1984; Terradas et al. 2008).
4. The onset of the instability generates vortices in the velocity field and disrupts the cross-sectional density profile and the magnetic field.
5. In the nonlinear regime, this can lead to turbulent-like flows developing through the oscillating flux tube, and ultimately plasma heating.

This process has been well studied in both analytical (e.g., Zaqarashvili et al. 2015; Barbulescu et al. 2019; Hillier et al. 2019; Hillier & Arregui 2019; Van Doorsselaere et al. 2021) and numerical settings (e.g., Antolin et al. 2014, 2015, 2018; Magyar & Van Doorsselaere 2016; Karampelas & Van Doorsselaere 2018; Afanasyev et al. 2019; Antolin & Van Doorsselaere 2019). The small spatial scales that form and the misalignment of magnetic field lines at the boundaries of Kelvin–Helmholtz

vortices can drive plasma heating (Karampelas et al. 2017) and lead to magnetic reconnection (Howson et al. 2021). Due to the nature of the fundamental standing waves (perturbed velocities/ magnetic field largest at apex/footpoints), small scales in the velocity field tend to generate viscous heating at the loop apex, while small scales in the magnetic field typically produce ohmic heating at the loop footpoints (e.g., Karampelas et al. 2017). A detailed review of the existing literature in this area is presented in Howson (2022).

In Hillier et al. (2020), the authors argued that observed kink wave amplitudes are not typically sufficient to balance expected energy loss rates. Despite this, in a recent paper, Shi et al. (2021) demonstrated that through this process, energy injected by a continuous, resonant driver, could lead to wave heating rates that were sufficient to balance radiative losses. However, the value used for the loop density by Shi et al. (2021) is relatively low, more appropriate for Quiet Sun loops than active region loops. In this article, we consider whether this result generalizes to higher-density structures (for example, active region loops) and to nonresonant drivers. In Section 2, we describe our model, in Section 3 we present our results, and in Section 4 we provide a discussion of our findings. Finally, in Section 5, we draw some concluding remarks.

2. Model Setup

2.1. Initial Setup

Our model loop is based on a 3D flux tube setup in the corona, with our model parameters representative of the Quiet Sun corona. The model parameters are also chosen to correspond to the model studied by Shi et al. (2021), to allow for a direct comparison with results presented by these authors. The 3D coronal flux tube consists of a straight, cylindrical density enhancement, which is embedded in a vertical magnetic field. The magnetic field is initially aligned with the z-direction and the background density profile is defined as

$$\rho = \rho_e + \frac{\rho_i - \rho_e}{2}\{1 + \tan h(ar - b)\}. \qquad (1)$$

Here $r = \sqrt{x^2 + y^2}$, $\rho_{e,i}$ are the exterior and interior densities, and a and b are constants that define the flux tube radius and the width of the boundary layer, respectively. The values of a and b were selected such that the loop radius is 1 Mm and the boundary thickness is approximately 0.4 Mm. The loop has a length of 200 Mm. This loop sits within a numerical domain of dimensions $-4 \leqslant x, y \leqslant 4$ Mm and $0 \leqslant z \leqslant 200$ Mm. We use $512 \times 512 \times 100$ grid points, in the x-, y- and z-directions, respectively.

We will consider two different scenarios for the density. In the first one, the external density is set to be $\rho_e = 1.67 \times 10^{-12}$ kg m^{-3} whereas in the second, we reduce the density by an order of magnitude such that $\rho_e = 1.67 \times 10^{-13}$ kg m^{-3}. The lower density corresponds to the setup described in Shi et al. (2021). For both cases, the ratio between the internal and external density is a factor of 3 ($\rho_i/\rho_e = 3$), resulting in densities in the central core of the flux tubes of $\sim 5 \times 10^{-12}$ kg m^{-3} in the higher-density case and $\sim 5 \times 10^{-13}$ kg m^{-3} in the lower-density loop. Figures 1 and 2 show a vertical cut and horizontal cross section of this density profile for the higher-density case. For the remainder of this article, we refer to the uniform, internal density region as the core of the loop and the transition layer (given by the tan$h$ profile) as the shell region.

The initial temperature of both the interior and exterior plasma is set to 1 MK, implying the gas pressure is not uniform across the loop. Therefore, in order to maintain total pressure balance for an initial equilibrium, the strength of the magnetic field within the density-enhanced flux tube is reduced. We note that as we are modeling a low β plasma, the interior field strength is only reduced by a small amount ($\sim 0.7\%$) relative to the background strength (30 G).

For the simulations discussed within this article, we used the numerical code Lare3D (Arber et al. 2001). This scheme advances the full, resistive, 3D, MHD equations in normalized form. The equations are given by

$$\frac{D\rho}{Dt} = -\rho\nabla \cdot \boldsymbol{v}, \qquad (2)$$

$$\rho\frac{D\boldsymbol{v}}{Dt} = \boldsymbol{j} \times \boldsymbol{B} - \boldsymbol{\nabla}P - \rho\boldsymbol{g} + \boldsymbol{F}_{\text{visc.}}, \qquad (3)$$

$$\rho\frac{D\epsilon}{Dt} = -P(\nabla \cdot \boldsymbol{v}) - \rho^2\Lambda(T) + \eta|\boldsymbol{j}|^2 + Q_{\text{visc.}} + Q_{\text{bg.}}, \qquad (4)$$

$$\frac{D\boldsymbol{B}}{Dt} = (\boldsymbol{B} \cdot \nabla)\boldsymbol{v} - (\nabla \cdot \boldsymbol{v})\boldsymbol{B} - \boldsymbol{\nabla} \times (\eta\boldsymbol{\nabla} \times \boldsymbol{B}), \qquad (5)$$

$$P = 2k_B nT. \qquad (6)$$

Here, ρ is the plasma density, $\boldsymbol{v}$ is the velocity, $\boldsymbol{j}$ is the normalized current density ($\boldsymbol{j} = \boldsymbol{\nabla} \times \boldsymbol{B}$), $\boldsymbol{B}$ is the magnetic field, P is the gas pressure, and ϵ is the specific internal energy. We include the effects of optically thin radiation ($\lambda(T)$) and a uniform background heating ($Q_{\text{bg.}}$) in the energy Equation (4). This heating term is set such that the temperature outside the loop is maintained at its initial temperature of 1 MK. This is not sufficient to maintain the coronal temperatures inside the loop because the higher density inside the loop implies radiation will be more efficient here. Hence, without additional heating, we would expect the core of the loop to cool.

In the equations above, we also include the effects of non-zero magnetic diffusivity and shock viscosity terms. The magnetic diffusivity is approximately 2×10^8 m^2 s^{-1}. Due to well-known numerical constraints, this is necessarily many orders of magnitude larger than the value expected within a typical coronal plasma. However, the value of the magnetic diffusivity used in these simulations is as small as possible while being larger than numerical diffusivity so we retain control over the diffusion and it is not simply determined by the resolution of the simulations (see also, e.g., Bingert & Peter 2011; Reale et al. 2016; Rempel 2017; Daldorff et al. 2022). The shock viscosities contribute to both the momentum equation in the form of a viscous force ($\boldsymbol{F}_{\text{visc.}}$) and to the energy equation as viscous heating ($Q_{\text{visc.}}$). They are included to ensure numerical stability and are described in detail in Arber (2018). We note that as the KHI is sensitive to the transport coefficients (Howson et al. 2017), the simulation dynamics and observed heating rate will be strongly affected by these values.

2.2. Boundary Conditions

In this paper, we consider the results of MHD wave simulations in which transverse modes are excited by a velocity driver of the form $v_y = v_0 \sin(\omega t)$ imposed on the lower z boundary. In our model setup, this boundary would correspond to the coronal boundary, where we consider these coronal boundary perturbations as arising of photospheric footpoint motions. We consider two different cases where we
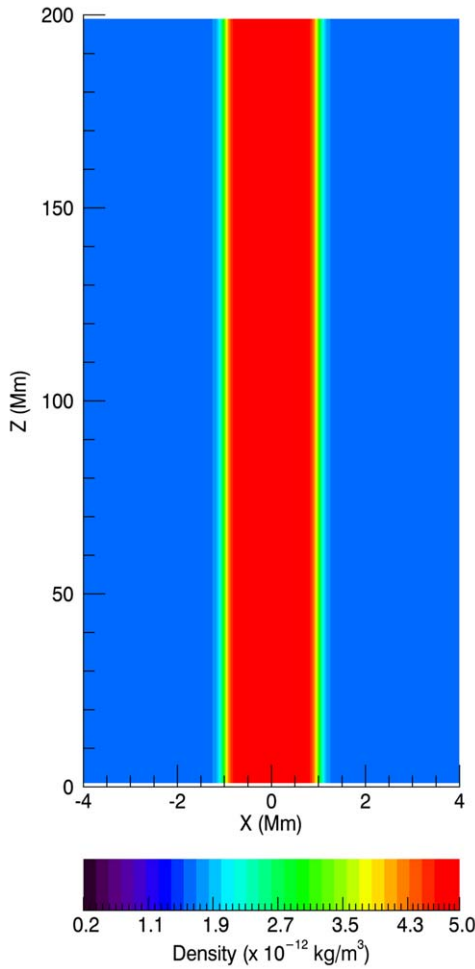
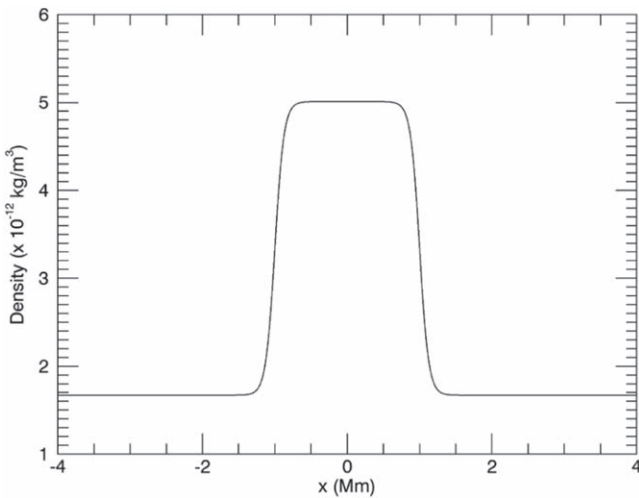**Figure 1.** A vertical cross section of the initial density (i.e., at $t = 0$ s).

Figure 2. A horizontal cross section of the initial density (i.e., at $t = 0$ s).

vary the frequency of the driver, ω to be either "tuned" (to induce a resonant oscillation) or "detuned" (leading to a nonresonant oscillation of the flux tube). In particular, for a tuned driver, the flux tube is driven with the fundamental kink frequency of the system (see for example Edwin & Roberts 1983; Nakariakov & Verwichte 2005). Using the
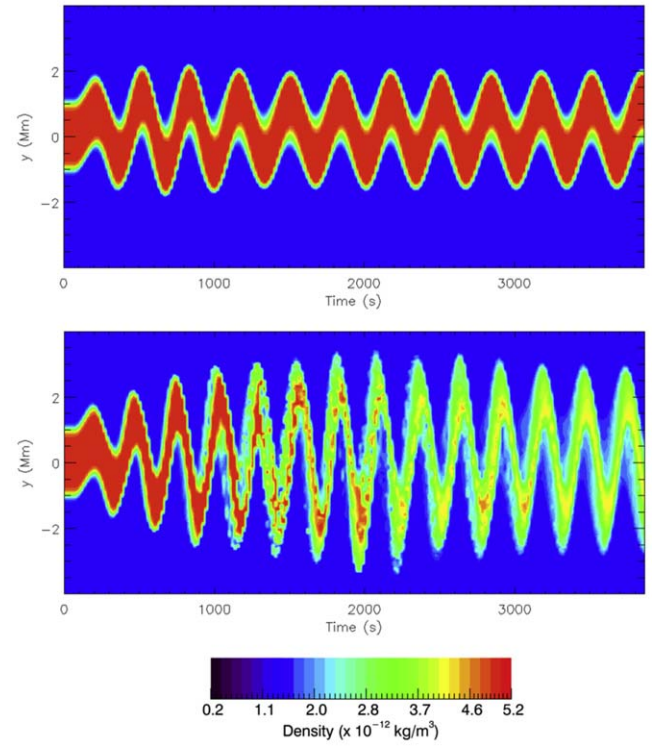

Figure 3. Time-distance plots of the density (nondimensional units) at the apex of the loop ($z = 100$ Mm and $x = 0$ Mm). The top panel shows the evolution of the density for the detuned simulation whereas the bottom panel corresponds to the tuned driver. For both simulations, the densities correspond to the higher-density setup (i.e., where $\rho_e = 1.67 \times 10^{-12}$ kg m^{-3}).

standard expression for the kink speed (see for example, Equation (8) in Nakariakov & Verwichte 2005), the resonant periods used in our study correspond to 273 s for the high-density model ($\rho_e = 1.67 \times 10^{-12}$ kg m^{-3}) and 86.3 s for the low-density setup ($\rho_e = 1.67 \times 10^{-13}$ kg m^{-3}), respectively. In all cases, the amplitude of the driver is $v_0 \sim 8$ km s^{-1} at the lower ($z = 0$ Mm) boundary.

At the upper z boundary, waves are reflected back into the domain using zero gradient conditions. At the lower z boundary, we impose $v_x = v_z = 0$ (the form of v_y is described above) and enforce zero gradients in the plasma parameters. The x and y boundaries are periodic.

3. Results

3.1. Effect of Driving Frequency

In a first set of simulations, we compare two setups using the higher-density model (i.e., where $\rho_e = 1.67 \times 10^{-12}$ kg m^{-3}) but change the period of the driver. Optically thin radiation is not included in these simulations and hence, there is also no background heating. The boundary driving continues for the duration of the simulations. As the simulations start, the driver at the lower boundary excites transverse oscillations of the flux tube, which propagate into the domain. To indicate the movement of the flux tube, the evolution of the density at the apex of the loop is shown in Figure 3 as time-distance graphs for both simulations. It is immediately obvious from the two panels that the evolution of the loop is substantially different in both simulations. Within 2–4 periods, the resonant simulation (tuned driver—bottom panel) clearly shows a growth in the
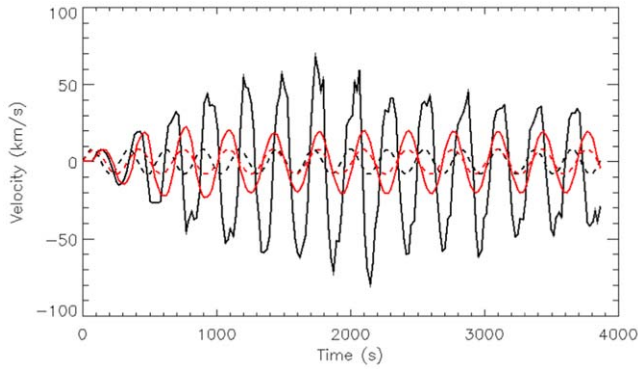
Figure 4. The transverse velocity in the midpoint of the domain ($x = y = 0$ Mm, $z = 100$ Mm) as a function of time. The black lines correspond to the tuned driver whereas the red lines represent the detuned driver. For comparison, the dotted lines show the corresponding transverse velocity of the driver on the lower boundary ($x = y = z = 0$ Mm). For both simulations, the densities correspond to the higher-density setup.

amplitude of the loop displacement. This can also be seen from Figure 4 where the black lines shows the rapid growth of the transverse velocity for the tuned simulation, from a value of 8 km s^{-1} at the driven boundary (black dashed line) to a maximum of about 70 km s^{-1} at the apex of the loop (solid black line). In addition to the increasing amplitude of the displacements, the bottom panel of Figure 3 also shows fragmentation of the density at the loop apex for the tuned simulation. Due to the radial density profile, resonant absorption (or mode coupling) occurs and the large velocity shears in the boundaries of the flux tube lead to the development of the KHI. The KHI mixing also leads to an increase in the cross-sectional area of the flux tube, resulting in a general decrease of the density at later times. When the driver is not tuned to induce resonance (top panel), the amplitude of the flux tube displacement remains constant (see also red lines in Figure 4 for the corresponding transverse velocity evolution) and as the KHI is no longer strongly induced, there is no fragmentation of the density profile. For the tuned driver, we see a decrease of the transverse velocity (solid black line Figure 4) at later times as the system "detunes" due to the KHI and other nonlinear effects.

3.2. Effect of the Density

In the next set of simulations, we compare the effect of the different density models. As a reminder, we refer to the model with $\rho_e = 1.67 \times 10^{-13}$ kg m^{-3} as the "lower-density" and the "higher-density" model corresponds to $\rho_e = 1.67 \times 10^{-12}$ kg m^{-3}. Both models have a density ratio $\rho_i/\rho_e = 3$. For these simulations, optically thin radiation is included for the full duration of the simulation, together with a uniform background heating that balances the radiation outside the loop. However, without additional heating provided by the dissipation of wave energy, the denser loop is expected to cool as the background heating is not sufficient to compensate the higher radiative losses in the loop core.

The left-hand column of Figure 5 shows the evolution of a cross section of the density at the loop apex as time-distance graphs for three simulations. The top panel corresponds to a simulation with the lower-density model and where the driver has been tuned to be resonant for this particular loop setup. The middle panel also corresponds to the lower-density model but the driver is now detuned. The simulation represented in the

bottom panel again has a tuned driver but now considers the higher-density setup. This combination of setups gives an "optimal" scenario where the driver is most efficient (tuned) and radiation is weak (lower density), a scenario where the driver is not tuned (and hence perhaps more representative of random footpoint motions) but where the radiation is still weak and finally, a scenario where the driver is optimized but radiation is stronger due to the higher density. The different setups naturally have different frequencies, associated with the different drivers tuned/detuned to the relevant resonant kink frequency of the system. In general though, we see the same pattern in these time-distance plots as discussed for the tuned and detuned simulations in Figure 3; for the tuned (resonant) driver, we see an increase in amplitude of the perturbation at the loop apex and fragmentation of the density. However, for the higher-density, tuned-driver case, we see a substantial increase in the density at the loop apex over time (see lower left panel of Figure 5). Here, the enhanced radiative losses encourage the formation of a region of dense, cool plasma so despite the increase in the loop cross-sectional area (due to the KHI), the time-distance diagram shows an increase in density in this case.

Figure 6 shows the evolution of the maximum and mean temperatures in the 3D simulation domain for the three simulations. We can see that the low-density setup with a tuned driver does indeed represent an "optimal" scenario where the dissipation of the boundary-driven transverse waves leads to a significant increase of the maximum temperature (to just below 1.8 MK). However, even in this case, the mean temperature in the domain remains roughly constant, increasing to only just above the initial temperature of 1 MK (see also discussion of Figure 7 below). From the top right-hand panel in Figure 5 we see that, as expected, the maximum temperatures occur in the loop boundary where the wave heating is most efficient due to phase mixing and the small length scales associated with the KHI. On the other hand, the reduced heating rates and enhanced radiative losses in the denser core of the loop, ensure the plasma cools here.

It is clear from the temperature evolutions in Figure 6 that the optimal scenario (tuned driver, lower density) is the only combination for which substantial heating takes place. When the density is increased by an order of magnitude (corresponding to a loop density of $\rho_i \approx 5 \times 10^{-12}$ kg m^{-3} and external density of $\rho_e = 1.67 \times 10^{-12}$ kg m^{-3}), the maximum temperature in the computational domain hardly increases (thin black lines) whereas the mean temperature (dashed thin black line) is decreasing significantly. Hence, even a driver chosen to be resonant cannot balance the higher radiative losses associated with the higher density for this particular setup. The bottom right-hand panel of Figure 5 does indeed show very rapid cooling of the core of the loop and despite the wave heating in the loop boundaries, radiation dominates and these regions gradually cool as well. Finally, the low-density simulation was repeated but with a detuned driver. For this combination, the maximum temperature remains more or less constant at 1 MK but the mean temperature is very gradually declining. This demonstrates that even for the low-density setup (loop density $\rho_i \approx 5 \times 10^{-13}$ kg m^{-3}), the driver needs to be optimally tuned to be able to provide sufficient energy to balance the radiative losses.

To provide further insight into the domain-integrated temperature profiles, Figure 7 shows horizontal (across the loop)
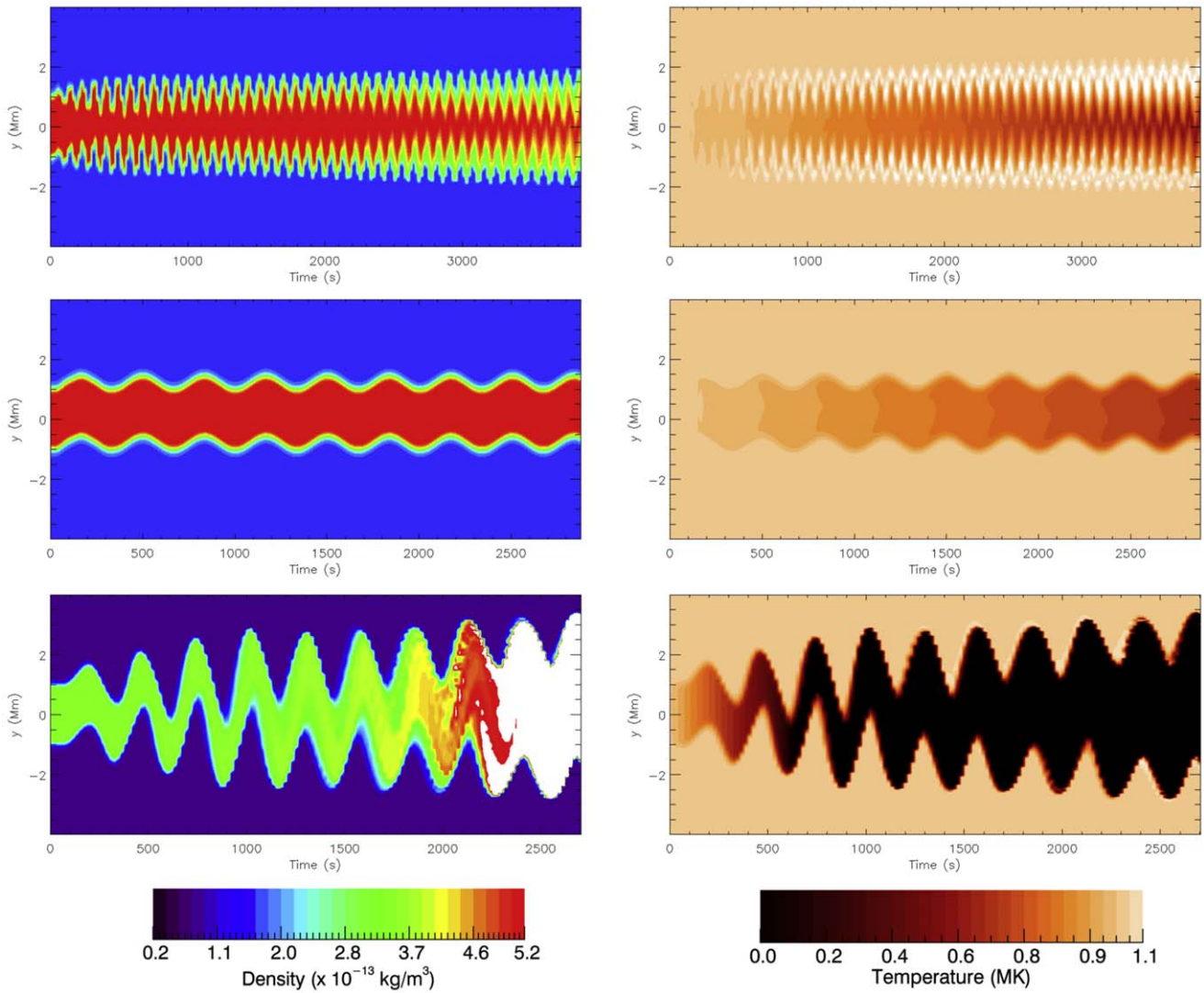
Figure 5. Time-distance plot of the density (left panels) and temperature (right panels) at the apex of the loop ($z = 100$ Mm and $y = 0$ Mm). The top two rows correspond to the lower-density simulations. The top panels have a tuned driver and the middle panels have a detuned driver. The bottom panels correspond to a tuned driver with the higher density. Note that to have comparable color tables, the density for the high-density simulation has been divided by 15.
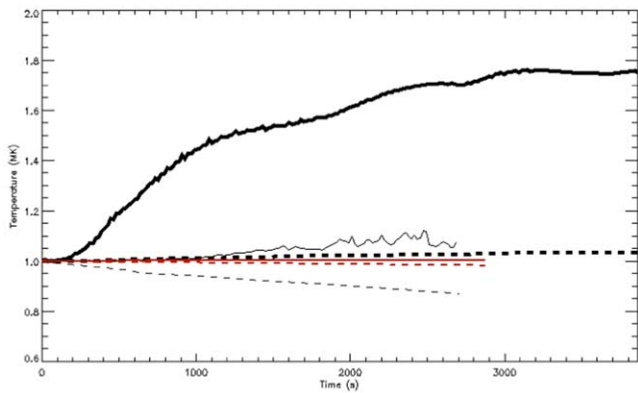

Figure 6. Evolution of the maximum (solid lines) and mean (dashed lines) temperatures in the 3D simulation volume. The thick black lines correspond to the low-density, tuned simulation, the thin black lines to the high-density, tuned simulation, and the red lines represent the low-density, detuned simulation. Optically thin radiation is included in all three cases.

cross sections of the temperature (top), density (2nd row), and vorticity (bottom row). Although Figure 6 showed a substantial increase in the maximum temperature in the simulation volume for the low-density, tuned simulation, these snapshots (left panels) make it clear that this corresponds to a strong but localized temperature increase in the shell region of the loop, as was also seen in the top-right panel of Figure 5. As summarized in the Section 1, the combination of resonant absorption, phase mixing, and KHI is expected to lead to the development of small spatial scales (strong gradients), leading in turn to increased efficiency in the dissipation of the wave energy. The small spatial scales are clearly visible in the horizontal cross sections at the loop apex, particularly in the shell region of the loop, with the cross section of the vorticity (bottom-left panel) confirming the presence of strong gradients in the velocity field in the shell region of the loop. The core of the loop though is still cooling, as without the strong gradients, the wave dissipation is not sufficiently efficient to balance the stronger
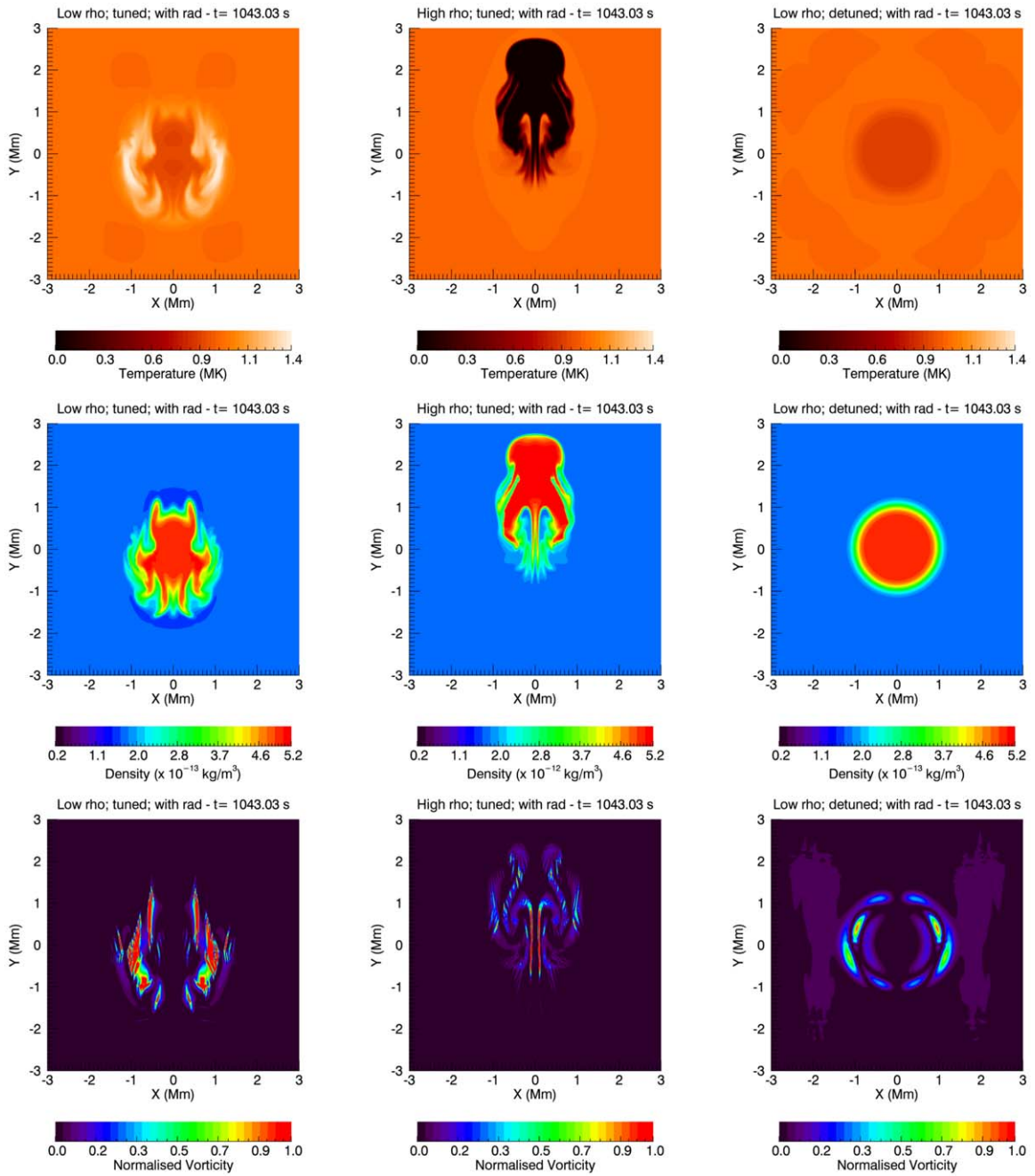
Figure 7. Horizontal cross sections at the loop apex ($z = 100$ Mm) at $t = 1043$ s of temperature (top row), density (2nd row), and vorticity (bottom row) for the low-density, tuned simulation (left panels) the high-density, tuned simulation (middle panels), and the low-density, detuned simulation (right panels). Note that to have comparable color tables, the density cross sections for the low-density simulations have been multiplied by three. The vorticity for the tuned simulations has been divided by 10^{-2} and by 10^{-7} for the detuned simulation (bottom right).

radiative losses in the denser loop core. The combination of the increased temperatures in the loop shell but cooler temperature in the core (together with the fact that the loop only occupies part of the simulation volume) explains the mostly constant mean temperature in Figure 6 for the low-density, tuned simulation.

The middle column of Figure 7 shows the corresponding cross sections for the higher-density, tuned simulation. It is clear that even with the most efficient (resonant) driver, the wave dissipation is not able to balance the increased radiative losses in the shell or the core of the loop. Despite KHI still developing, the temperature rapidly collapses to the

temperature floor in the simulation (set at $T = 2 \times 10^4$ K), even in the shell region of the loop. Finally, the right-hand panels show that for the low-density, detuned simulation, the transverse boundary driver does not deliver sufficient energy to cause substantial heating and the entire loop, including the shell region, gradually cools. This is consistent with the almost constant maximum temperature and slowly decreasing mean temperature in Figure 6 for this simulation (red lines). In summary, in all three cases, we find that the core of the loop cools, despite the presence of a weak background heating (only sufficient to balance the radiative losses in the lower-density loop environment) as wave dissipation is not efficient in this
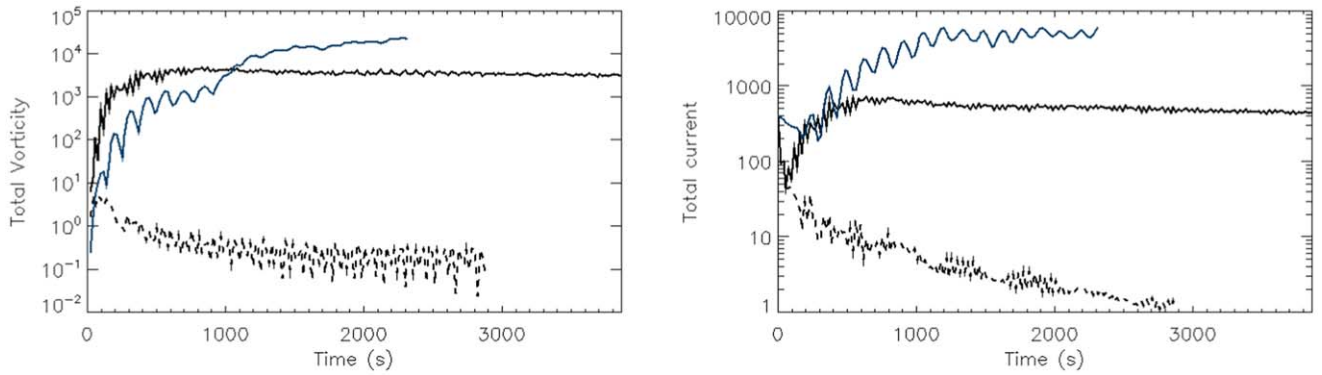
Figure 8. Evolution of the total (i.e., volume integrated) vorticity (left) and current (right) for the low-density, tuned simulation (solid black line), the high-density, tuned simulation (blue line), and the low-density, detuned simulation (dashed black line). Optically thin radiation is included in all three cases.
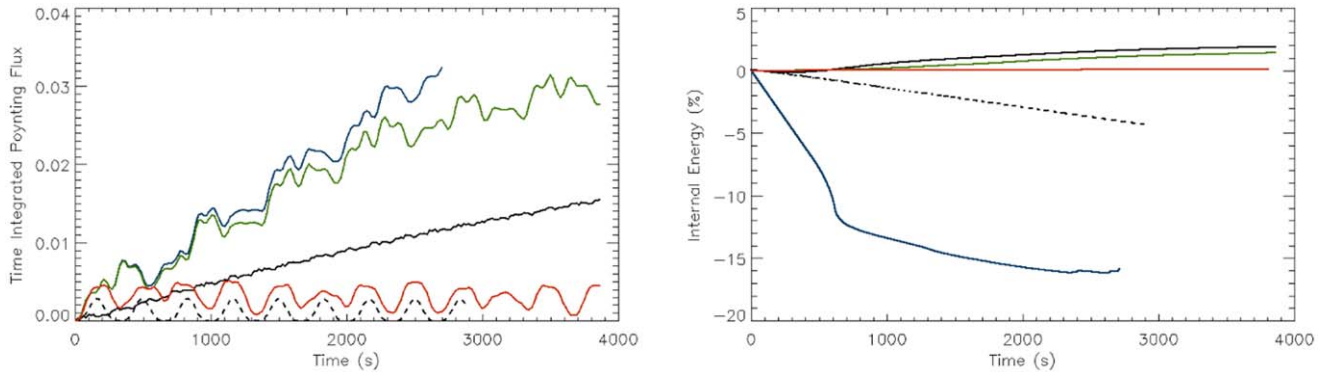

Figure 9. Evolution of the time-integrated Poynting flux (left) and internal energy in the 3D simulation volume (right). The colors correspond to the following simulations: black = tuned driver, low density, radiation included; green = tuned driver, high density, no radiation; red = detuned driver, higher density, no radiation; black dashed = detuned driver, low density, radiation included; blue = tuned driver, higher density, radiation included. Note that the internal energy plot shows the change in internal energy in the 3D domain, normalized against the initial internal energy.

region due to the lack of large gradients and the strong increase in temperature for the low-density, tuned simulation is localized in the shell of the loop.

The bottom row of Figure 7 shows horizontal cross sections of the square of the vorticity for the three simulations at time $t = 1043$ s. The left panel of Figure 8 shows the volume integrated vorticity squared. At later times, the vorticity keeps building in the high-density case as the loop is severely distorted by the KHI induced by the large-amplitude transverse perturbations. In the lower-density, tuned simulation, the vorticity levels off and then gradually declines, as the buildup in small scales is offset by the dissipation due to the (shock) viscosity. For the low-density, detuned simulation (black dashed line), the vorticity never really builds up due to the lack of velocity shear building up in the shell regions. The right-hand panel of Figure 8 shows the volume-integrated current squared, which behaves very similar to the vorticity.

4. Discussion

Using 3D simulations of wave heating in closed flux tubes, we have shown that wave heating is able to balance radiative losses in coronal loops (see also Shi et al. 2021), but only in an optimal scenario with a lower density (more appropriate for Quiet Sun loops than active region loops) to avoid rapid cooling due to radiation and a driver tuned to be resonant. A key difference between the tuned and detuned simulations is the amount of energy that is injected into the domain. As demonstrated by, e.g., Prokopyszyn et al. (2019) and

Prokopyszyn & Hood (2019), only a resonant driver will lead to a net increase in the Poynting flux; as a resonance is set up, the driver consistently enhances the amplitude of the loop oscillation. As such, the wave driver injects energy efficiently into the computational domain. However, for the nonresonant driving, the imposed velocity is frequently acting in the opposite direction to the oscillation within the volume. Thus, the driver often removes energy from the system, restricting the growth in amplitude of the loop oscillation and resulting in a lower average Poynting flux. For our simulations, this is clearly seen in Figure 9, which shows the evolution of the time-integrated Poynting flux (left panel; where the Poynting flux is defined as $\mathcal{F} = -\int (\boldsymbol{E} \times \boldsymbol{B}) \cdot d\boldsymbol{S}$) and internal energy (right panel; using the expression for the internal energy $\epsilon = P/\rho$) for the five simulations included in this study. The green and red lines correspond to the higher-density, no-radiation simulations with a tuned and detuned driver, respectively. The black lines represent the low-density simulations, which include optically thin radiation (and a background heating term) with a tuned (solid black) and detuned (dashed black) driver. The blue line corresponds to the simulation, which again includes radiation, with a tuned driver but higher density.

Comparing the Poynting flux and internal energy confirms that only the combination of the lower-density setup and an optimal driver leads to an increase of energy when radiative losses are included. Although the green and red lines show an increase in the volume-integrated internal energy for the higher-density setup, there are no radiative losses (or
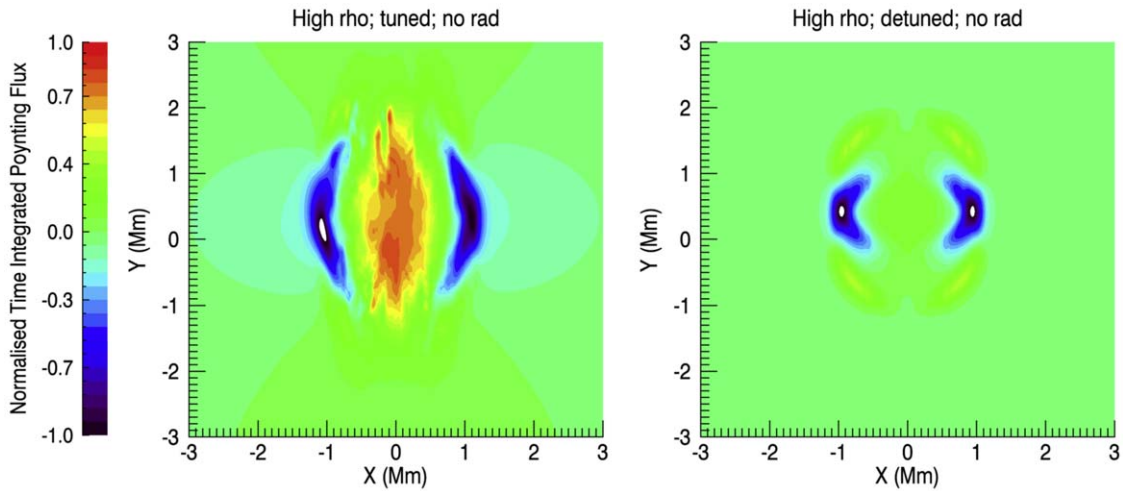
Figure 10. The time-integrated Poynting flux on the lower boundary for the tuned (left) and detuned (right) simulations. Positive values correspond to energy entering the domain.

background heating) included in these simulations. The green and blue lines provide a direct comparison for the higher-density simulation with a tuned driver both with and without radiation included. The catastrophic decrease of the blue line clearly indicates that the wave dissipation (combined with the weak background heating) is not able to balance the radiative losses despite the fact that the Poynting flux entering the domain for these two simulations is almost the same.

The black lines provide a direct comparison of the lower-density simulations for the tuned (solid) and detuned (dashed) simulations (radiation included). Here, the major difference is the Poynting flux entering the domain, which only builds up for the tuned simulation. In this case, the internal energy does build up over time, as the wave heating is able to balance the relatively weak radiative losses associated with the lower density. However, from the detailed analysis of the spatial structure of the temperature (see, e.g., Figures 5 or 6) we know that even in this case, the increase in temperature is limited to the shell region of the loop, with the higher-density core of the loop still cooling.

Given the spatial structuring of the temperature evolution in the loop, it is worthwhile also looking at the spatial distribution of the Poynting flux. Figure 10 shows the time-integrated Poynting flux on the lower (driven) boundary for detuned (right) simulations. In this representation, positive values correspond to energy being injected into the simulation volume. Initially, both drivers inject energy into the domain as they drive transverse (kink) waves. Ultimately, the resonant driver will inject significantly more energy into the simulation volume than for the nonresonant case, as confirmed by the time-integrated Poynting flux in Figure 9. Figure 10 shows that the cumulative Poynting flux has significant spatial variation on the lower boundary. In both cases, we see energy is removed in the shell region. For the tuned case, we see that substantial energy is injected within the core of the loop whereas in the detuned case, there is minimal Poynting flux entering the domain. The persistence of the transverse kink mode in the loop core permits continued resonance and thus allows a sustained inflow of energy here. In the boundary however, resonant absorption leads to the generation of azimuthal Alfvén waves. While these have the same frequency as the global kink mode, they are out-of-phase with the oscillation of the loop core. As such, the
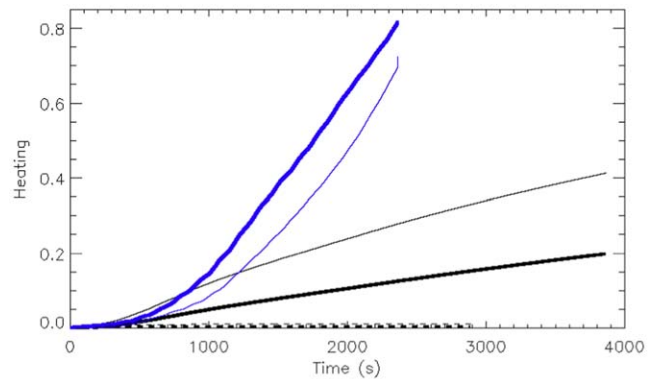

Figure 11. Evolution of the ohmic heating (thick lines) and heating resulting from the shock viscosities in Lare3D (thin lines). The colors correspond to the following simulations: black = tuned driver, low density, radiation included; black dashed = detuned driver, low density, radiation included; blue = tuned driver, higher density, radiation included.

imposed velocity driver opposes the azimuthal mode and thus consistently removes energy from the loop boundaries.

Figure 11 shows the nature of the heating that is present in the (radiative) simulations, with the solid lines representing the ohmic heating and the dashed lines the Lare viscous shock heating. Both of these will be most efficient in regions where small spatial scales (i.e., large gradients) are able to build up. Although only the volume-integrated quantities are shown here, as in Shi et al. (2021), the ohmic heating associated with higher currents mostly builds away from the apex of the loop whereas the viscous heating will dominate at the apex, where the velocity perturbations are largest.

From the heating/cooling behavior and the density profiles, we can make an estimate of how the wave heating compares with the background heating (which is only sufficient to maintain the temperature outside the loop). Given the shell region of the low-density, tuned-driver loop is increasing in temperature, the combination of the wave heating and background heating is sufficient there to offset the radiative cooling. As the heating requirement must scale with at least the square of density (as we know the cooling does), the wave heating in the shell region of the loop (where the density is roughly double of the loop environment) must be at least three times
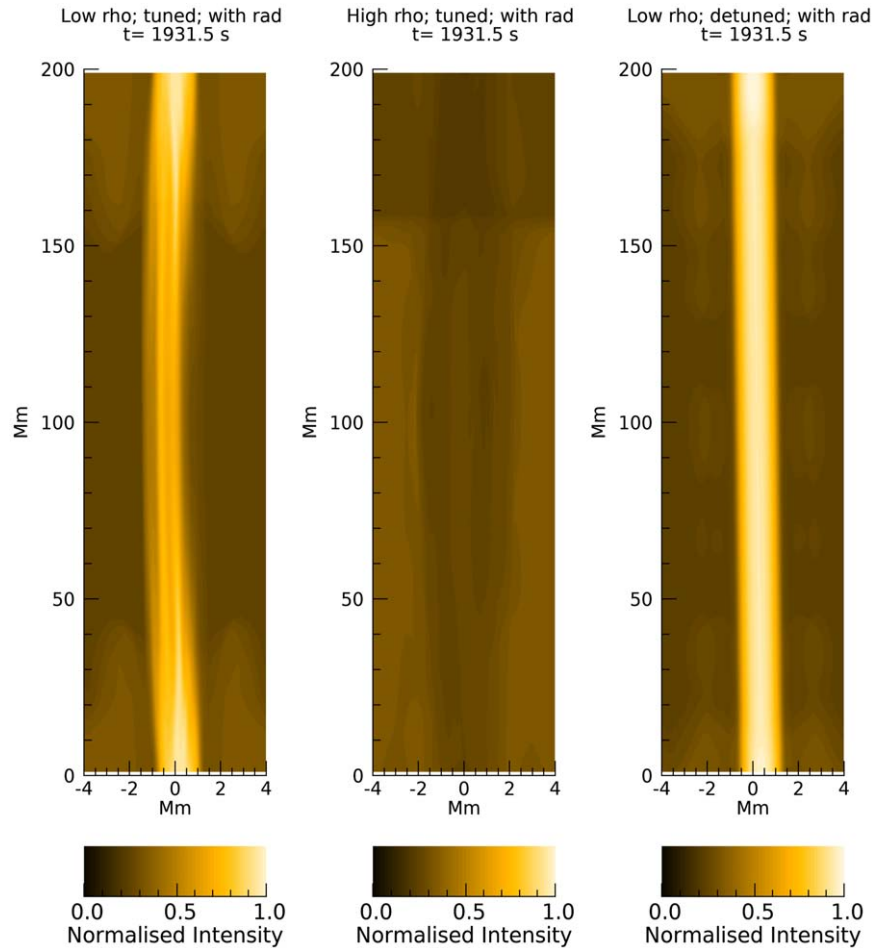
Figure 12. AIA 171 Å (normalized) intensity along a line of sight perpendicular to the loop at time = 1931 s, for the low-density tuned simulation (left), the high-density, tuned simulation (middle), and the low-density, detuned simulation (right). In each case, the intensity has been normalized to the maximum intensity at the start of the simulation.

larger than the background heating for the low-density, tuned-driver simulation (so that the background heating plus the wave heating is at least four times higher than the background heating alone).

5. Conclusions

In summary, by comparing resonant and nonresonant boundary driven transverse waves in a coronal loop with a radial density profile, we find that wave heating associated with a driver tuned to be resonant in a lower-density loop (where the loop core has a density of $\sim 5 \times 10^{-13}$ kg m^{-3}) is able to balance radiative losses. However, only for a (continuous) resonant driver is there a significant Poynting flux into the numerical domain. As such, nonresonant drivers cannot maintain the plasma temperature within the loop. Even for resonant driving, wave heating is not sufficiently efficient to balance the stronger radiative losses in a higher-density loop model (where the loop core has a density of $\sim 5 \times 10^{-12}$ kg m^{-3}). In this optimal scenario of lower density and a tuned driver, the heating mainly occurs in the shell, rather than the core, region of the loop and hence heating will only spread through the entire volume of the loop if the KHI is able to disrupt the full cross section of the loop. We also note here that we have only included (optically thin) radiative losses whereas in reality, there will be additional losses from thermal conduction. Although the value of magnetic

diffusivity used in these simulations might result in a larger diffusion than would be expected in the corona, this implies that our results can be considered a best case scenario. For lower resistivity, we would get even less heating.

In our setup, the resonant simulation showed velocities at the apex of the loop up to 70 km s^{-1}. Estimates of coronal velocities based on observed nonthermal line broadening are typically somewhat smaller, with maximum values up to about 50 km s^{-1} reported in the literature (e.g., McIntosh & De Pontieu 2012; Brooks & Warren 2016). The large amplification of the velocity we find at the apex of the loop is a direct consequence of the idealized setup in this study where the footpoint motions are driven at the resonant frequency, in a consistent direction. Relaxing these restrictions, for example by considering randomly directed footpoint motions and/or a broadband spectrum, might lead to lower apex velocities but potentially, also, to less efficient heating. In that sense, the model presented here is again a "best case" scenario. However, it is also possible that observations at higher spatial resolution than is currently achievable will lead to higher nonthermal line widths (e.g., Testa et al. 2016) and as such, based on the current upper estimate of 50 km s^{-1}, the value of about 70 km s^{-1} at the apex of our model loop is not inconsistent with observations either.

Finally, in Figure 12, we present snapshots of the AIA 171 Å intensity, normalized for each case to the maximum intensity at the start of the relevant simulation. For the higher-density case

(middle panel), we see that due to the strong cooling, the initially bright loop (due to the higher density inside the loop) is no longer distinguishable from the environment in this passband. For the lower-density, tuned case, we see clear evidence in the intensity of the filamentary structure due to the deformation of the loop cross section by the KHI. We see slightly increased density at the footpoints where the loop structure is more coherent. Perhaps somewhat surprisingly, we see a relatively bright loop for the low-density, detuned case. Here, the loop structure has remained very coherent due to the lack of strong KHI, which due to the line-of-sight integration, enhances the intensity. In addition, due to the low-density, cooling at this time in the simulation is relatively weak and has not affected the temperature of the loop sufficiently for it to be no longer visible in this passband. The combination of the weak cooling and the coherent structure implies the intensity in this passband, and at this time, is actually higher than in the low-density, tuned case, which has stronger heating. This example provides a reminder that bright structures in intensity can signal an absence of cooling, as much as the presence of (ongoing) heating.

ORCID iDs

I. De Moortel ⓘ https://orcid.org/0000-0002-1452-9330
T. A. Howson ⓘ https://orcid.org/0000-0002-4895-6277

References

Afanasyev, A., Karampelas, K., & Van Doorsselaere, T. 2019, ApJ, 876, 100
Antolin, P., Okamoto, T. J., De Pontieu, B., et al. 2015, ApJ, 809, 72
Antolin, P., Schmit, D., Pereira, T. M. D., De Pontieu, B., & De Moortel, I. 2018, ApJ, 856, 44
Antolin, P., & Van Doorsselaere, T. 2019, FrP, 7, 85
Antolin, P., Yokoyama, T., & Van Doorsselaere, T. 2014, ApJL, 787, L22
Arber, T. D. 2018, LareXd User Guide, version 3.3 edn
Arber, T. D., Longbottom, A. W., Gerrard, C. L., & Milne, A. M. 2001, JCoPh, 171, 151
Arregui, I. 2015, RSPTA, 373, 20140261
Barbulescu, M., Ruderman, M. S., Van Doorsselaere, T., & Erdélyi, R. 2019, ApJ, 870, 108
Bingert, S., & Peter, H. 2011, A&A, 530, A112
Brooks, D. H., & Warren, H. P. 2016, ApJ, 820, 63
Browning, P. K., & Priest, E. R. 1984, A&A, 131, 283
Chandrasekhar, S. 1961, Hydrodynamic and Hydromagnetic Stability (Oxford: Clarendon)
Daldorff, L. K. S., Leake, J. E., & Klimchuk, J. A. 2022, ApJ, 927, 196
Davila, J. M. 1987, ApJ, 317, 514
De Moortel, I., & Pascoe, D. J. 2012, ApJ, 746, 31
De Pontieu, B., Carlsson, M., Rouppe van der Voort, L. H. M., et al. 2012, ApJL, 752, L12
Duckenfield, T. J., Goddard, C. R., Pascoe, D. J., & Nakariakov, V. M. 2019, A&A, 632, A64
Edwin, P. M., & Roberts, B. 1983, SoPh, 88, 179
Goossens, M. 2008, in IAU Symp. 247, Waves Oscillations in the Solar Atmosphere: Heating and Magneto-Seismology, ed. R. Erdélyi & C. A. Mendoza-Briceno (Cambridge: Cambridge Univ. Press), 228
Goossens, M., Andries, J., & Arregui, I. 2006, RSPTA, 364, 433
Grossmann, W., & Tataronis, J. 1973, ZPhy, 261, 217
Hasegawa, A., & Chen, L. 1974, PhRvL, 32, 454
Heyvaerts, J., & Priest, E. R. 1983, A&A, 117, 220
Hillier, A., & Arregui, I. 2019, ApJ, 885, 101
Hillier, A., Barker, A., Arregui, I., & Latter, H. 2019, MNRAS, 482, 1143
Hillier, A., Van Doorsselaere, T., & Karampelas, K. 2020, ApJL, 897, L13
Hollweg, J. V., & Yang, G. 1988, JGR, 93, 5423
Howson, T. 2022, Symm, 14, 384
Howson, T. A., De Moortel, I., & Antolin, P. 2017, A&A, 602, A74
Howson, T. A., De Moortel, I., & Pontin, D. I. 2021, A&A, 656, A112
Ionson, J. A. 1978, ApJ, 226, 650
Karampelas, K., & Van Doorsselaere, T. 2018, A&A, 610, L9
Karampelas, K., Van Doorsselaere, T., & Antolin, P. 2017, A&A, 604, A130
Khan, J. I., & Aurass, H. 2002, A&A, 383, 1018
Kim, S., Nakariakov, V. M., & Shibasaki, K. 2012, ApJL, 756, L36
Klimchuk, J. A. 2006, SoPh, 234, 41
Klimchuk, J. A. 2015, RSPTA, 373, 20140256
Magyar, N., & Van Doorsselaere, T. 2016, A&A, 595, A81
McIntosh, S. W., & De Pontieu, B. 2012, ApJ, 761, 138
Morton, R. J., Tiwari, A. K., Van Doorsselaere, T., & McLaughlin, J. A. 2021, ApJ, 923, 225
Nakariakov, V. M., & Verwichte, E. 2005, LRSP, 2, 3
Pant, V., Magyar, N., Van Doorsselaere, T., & Morton, R. J. 2019, ApJ, 881, 95
Parnell, C. E., & De Moortel, I. 2012, RSPTA, 370, 3217
Prokopyszyn, A. P. K., & Hood, A. W. 2019, A&A, 632, A93
Prokopyszyn, A. P. K., Hood, A. W., & De Moortel, I. 2019, A&A, 624, A90
Reale, F. 2014, LRSP, 11, 4
Reale, F., Orlando, S., Guarrasi, M., et al. 2016, ApJ, 830, 21
Rempel, M. 2017, ApJ, 834, 10
Ruderman, M. S., & Erdélyi, R. 2009, SSRv, 149, 199
Ruderman, M. S., & Roberts, B. 2002, ApJ, 577, 475
Shi, M., Van Doorsselaere, T., Guo, M., et al. 2021, ApJ, 908, 233
Terradas, J., Andries, J., Goossens, M., et al. 2008, ApJL, 687, L115
Testa, P., De Pontieu, B., & Hansteen, V. 2016, ApJ, 827, 99
Van Doorsselaere, T., Goossens, M., Magyar, N., Ruderman, M. S., & Ismayilli, R. 2021, ApJ, 910, 58
Van Doorsselaere, T., Srivastava, A. K., Antolin, P., et al. 2020, SSRv, 216, 140
Viall, N. M., De Moortel, I., Downs, C., et al. 2021, in Space Physics and Aeronomy, Volume 1, Solar Physics and Solar Wind, ed. N. E. Raouafi et al. (New York: Wiley), 35
Wilmot-Smith, A. L. 2015, RSPTA, 373, 20140265
Zaqarashvili, T. V., Zhelyazkov, I., & Ofman, L. 2015, ApJ, 813, 123